

Quantum Hall valley splitters in a graphene PN junction

M. Jo*,¹ P. Brasseur*,¹ A. Assouline,¹ G. Fleury,¹ H.-S. Sim^{††},² K. Watanabe,³ T. Taniguchi,³ W. Dumernpanich,¹ P. Roche,¹ D.C. Glattli,¹ N. Kumada,⁴ F.D. Parmentier,¹ and P. Roulleau^{†1}

¹*SPEC, CEA, CNRS, Université Paris-Saclay, CEA Saclay, 91191 Gif sur Yvette Cedex France*

²*Department of Physics, Korea Advanced Institute of Science and Technology, Daejeon 34141, Korea*

³*National Institute for Materials Science, 1-1 Namiki, Tsukuba, 305-0044, Japan*

⁴*NTT Basic Research Laboratories, NTT Corporation,
3-1 Morinosato-Wakamiya, Atsugi 243-0198, Japan*

(Dated: March 30, 2022)

Graphene is a very promising test-bed for the field of electron quantum optics. However, the most elementary building block of electron quantum optics, a fully tunable and coherent electronic beam splitter, is still missing. Here we demonstrate coherent and tunable electronic beam splitters realized in graphene that couple Quantum Hall edge channels with channels having opposite valley polarizations. The transmission of the, so-called, valley beam splitters can be tuned from zero to near unity, showing marked oscillations with gate voltage and magnetic field that are well accounted for by theoretical modelling. Robust electron quantum coherence is demonstrated by implementing two beam-splitters in a PN junction, which provide a fully tunable electronic Mach-Zehnder interferometer. The tunability allows us to unambiguously discriminate quantum interferences due to Aharonov-Bohm phases in the Mach-Zehnder from the gate-voltage or magnetic-field dependent oscillations of the transmission through a beam splitter. Having clearly identified the Mach-Zehnder interferences, we study their dependence on the beam-splitter transmission and the bias voltage applied to the interferometer, and compare the dependence with that observed in conventional GaAs/AlGaAs Mach-Zehnder interferometers. In particular, a similar lobe structure of the interference visibility versus the bias voltage is observed demonstrating the universality of decoherence mechanisms in both systems.

I. INTRODUCTION

The simple analogy between the propagation of electrons in a quantum circuit and that of photons in an optics setup has given rise to a field of condensed matter physics called electron quantum optics [1], which has led to significant advances in our understanding of the properties of a quantum electrical current. This is particularly true in the chiral and one-dimensional edge channels (ECs) of the quantum Hall effect, which can be viewed as the electronic analogue of fiber optics. In conventional GaAs/AlGaAs two-dimensional electron systems, these ECs can be combined with simple, electrostatically tuned structures such as quantum point contacts and quantum dots, respectively realizing the electronic equivalent of beam splitters and energy filters. This combination allows building more complex quantum circuits, for instance Mach-Zehnder (MZ) interferometers [2], which give a direct access to the coherence properties of electronic wavepackets propagating in an EC [3].

Beyond GaAs/AlGaAs heterostructures, graphene is considered a very promising material for implementing electron quantum optics experiments. Indeed, not only is it expected to present more robust coherence properties than in conventional systems [4], but the presence of the valley degree of freedom provides an alternative way to encode information. Recently, valleytronics in two-dimensional layered materials with broken spatial inversion symmetry has generated a lot of interest [5, 6]. For

example, optical control of the valley isospin has been demonstrated in monolayer MoS₂ [7], and the pure valley current [8] and the domain wall effects [9, 10] have been observed in a biased bilayer graphene. Valleytronics in monolayer graphene has been less studied [11] in experiments because of the difficulty in manipulating valley isospin by electrostatic means—the inversion symmetry cannot be broken by usual gate voltage that generates electrostatic potential smoothly changing on an atomic distance scale. Unlocking this issue is valuable, since the difficulty implies the robustness of the valley isospin, a crucial merit of valleytronics in monolayer graphene. Valley isospin scattering at graphene edge is a way of resolving the difficulty. This has been theoretically predicted [12–14] in a PN junction in the quantum Hall regime. However, a way to control the isospin scattering at an edge has not been established, which hampers the full control of a valley state.

In this article, we present electronic beam splitters that directly rely on the valley degree of freedom of graphene. The principle of our valley beam splitters is based on the theoretical work of [12, 13], where the crystalline structure on the corner of a graphene PN junction allows scattering of electrons between PN interface channels, having opposite valley polarization, and quantum Hall ECs. We control this scattering by tuning the EC mixing point along the edge of the graphene flake using small electrostatic side gates, and we show that the resulting electronic transmission of the valley beam splitters can be reliably changed from zero to near unity, displaying sta-

ble and reproducible oscillations with side gate voltage and magnetic field. We develop a theoretical model explaining that these oscillations correspond to a spatial shift of the mixing point over one hexagonal lattice cell, and that their periodicity and amplitude are affected by edge roughness. We then use two valley beam splitters to form, in a controlled fashion, an electronic MZ interferometer along the p-n junction. Our ability to tune both valley beam splitters up to total reflection allows us to clearly separate the conductance oscillations due to the Aharonov-Bohm flux enclosed by the MZ from the ones due to the valley beam splitters, shedding light on the various oscillatory regimes observed in previous experiments [15–18]. From there we can probe the dependence of the visibility of the MZ interferences with the valley beam splitters transmission and the bias voltage, and compare it to the behavior commonly observed in GaAs/AlGaAs MZ interferometers. The ability to control the scattering of electrons involving PN interface channels having different valley polarizations can be viewed as a way to, in effect, directly act upon their valley degree of freedom. This makes our valley beam splitters an interesting prospect for valleytronics, a new field of electronics which, in a manner akin to spintronics, aims at encoding information in the valley[5, 6].

II. EXPERIMENT

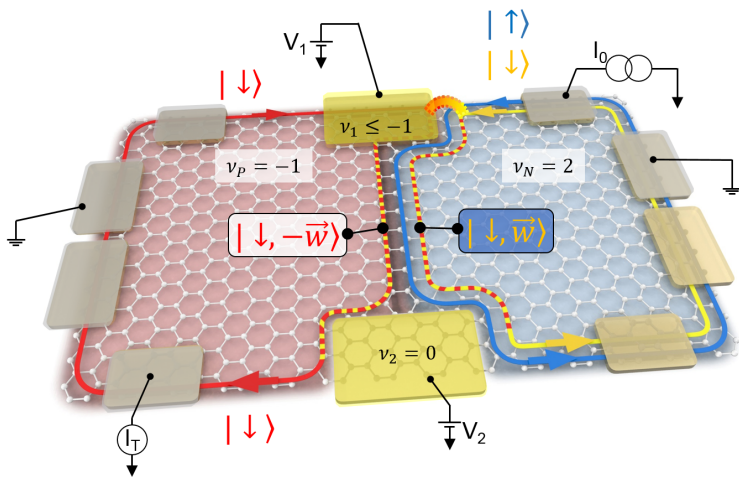


Figure 1: **Quantum Hall valley Splitter.** Schematic representation of the PN junction. The N region is depicted in blue, the P one in pink. Electrons are injected from the upper right ohmic contact (defining an injected current I_0) and transmitted current I_T is measured at the lower left contact. Buried ohmic contacts enable to simultaneously tune the filling factor by measuring the two-points Hall resistance on both sides of the junction.

The sample is in a bipolar quantum Hall state, as

shown in Fig.1. In the N region the Landau-level filling factor is $\nu_N = 2$ and two channels of the opposite spin (\uparrow, \downarrow) circulate counterclockwise along the boundary, while in the P region $\nu_P = -1$ and one spin-down channel circulates clockwise. Along the top edge, the injected current I_0 is carried by the two edge channels of the N region. Half of the current, resulting from spin up carriers, cannot flow to the P region, because of large energy cost for spin flip. The other half $I_0/2$ with spin down carriers, on which we focus hereafter, can contribute to the transmitted current I_T .

The flow of the spin-down current involves splitting into PN-interface channels that have opposite valley isospin [16, 19]. After passing the intersection between the top edge and the PN interface, the current flows along the P side of the interface with transmission probability $T_1 = |t_1|^2$ or the N side with reflection probability $|r_1|^2 = 1 - T_1$. The N-side and P-side currents have opposite valley isospins $\pm\vec{w}$ since valley degeneracy is lifted[20] under the strong perpendicular magnetic field in the bulk, hence the probability T_1 shows the degree of the valley-channel splitting. This is described by a quantum-mechanical superposition

$$|\Psi_{\text{initial}}\rangle = r_1|\downarrow, \vec{w}\rangle + t_1|\downarrow, -\vec{w}\rangle \quad (1)$$

of the N-side spin-down interface state $|\downarrow, \vec{w}\rangle$ and P-side state $|\downarrow, -\vec{w}\rangle$. Valley-isospin change from that of the top edge channel to $\pm\vec{w}$, which is a large momentum change, and occurs due to the atomic structure at the intersection[13].

III. QUANTUM HALL VALLEY SPLITTER

We develop a valley splitter in which the transmission probability T_1 and the valley isospin are controlled by electrical means. For this aim, we fabricated two small side gates on the intersections between the graphene physical edge and the PN interface (see Fig.1). Voltages applied on the side gates modify the profile of the electrostatic potential at both ends of the PN interface. When the filling factor below a side gate is set to $\nu \leq -1$, the PN junction intersects the physical edge, where the sharp potential change in atomic distance scale facilitates the valley-channel splitting. On the other hand, when the filling factor is set to $\nu = 0$, the PN junction intersects an electrically defined edge, where the potential change is smooth and the valley isospin does not change.

We first demonstrate that the transmission probability T_1 , defined as $T_1 = I_T/(I_0/2)$, can be tuned by changing the voltage V_1 applied on the top side gate (see Figs. 2a and 2b). By setting $\nu_1 \leq -1$ below the top side gate and $\nu_2 = 0$ below the bottom side gate, we expect that the valley-channel splitting occurs at the top intersection but not at the bottom (see the channel splitting shown in Fig.1). For $V_1 > 0$ (Fig. 2a), ν_1 is equal to zero, and the PN junction only intersects electrostatically defined edges. This fully suppresses valley-channel

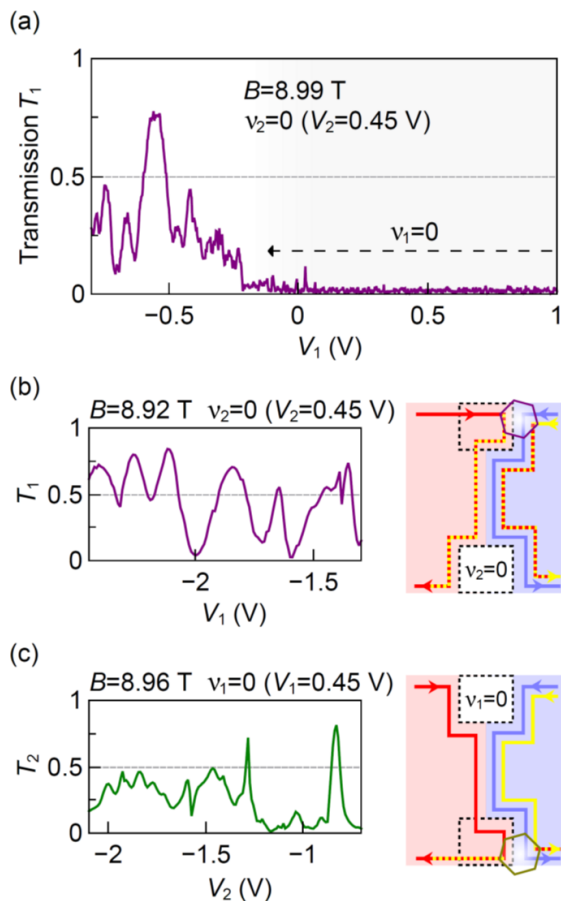


Figure 2: **Oscillations of the quantum Hall valley splitter.** (a) Measured transmission as a function of the top side gate voltage V_1 , for $\nu_2 = 0$ below the bottom side gate. For $\nu_1 = 0$ below the top side gate (dashed arrow), the injected current is fully reflected. For $\nu_1 < 0$, current can be transmitted. (b) Measured transmission T_1 of the top beam splitter as a function of V_1 for $\nu_1 \leq -1$ below the top side gate and $\nu_2 = 0$ below the bottom side gate. Right panel: sketch of the corresponding edge states configuration. The splitting point is symbolized by the purple hexagon. (c) Measured transmission T_2 of the bottom beam splitter as a function of V_2 , for $\nu_2 \leq -1$ below the top side gate and $\nu_1 = 0$ below the top side gate. Right panel: sketch of the corresponding edge states configuration. The splitting point is symbolized by the green hexagon.

splitting, and the measured transmission vanishes. Conversely, for $V_1 < 0$, $\nu_1 \leq -1$ and the PN junction intersects the top physical edge: valley-channel splitting now occurs at the top intersection only, leading to a finite transmission. We show in Fig. 2b that the transmission probability T_1 can be tuned between zero and almost unity by changing the voltage V_1 (importantly, T_1 can also be tuned by changing the magnetic field, see *e.g.* Fig. 4a). The period of the V_1 dependence is $\Delta V_1 \sim 100$ meV on

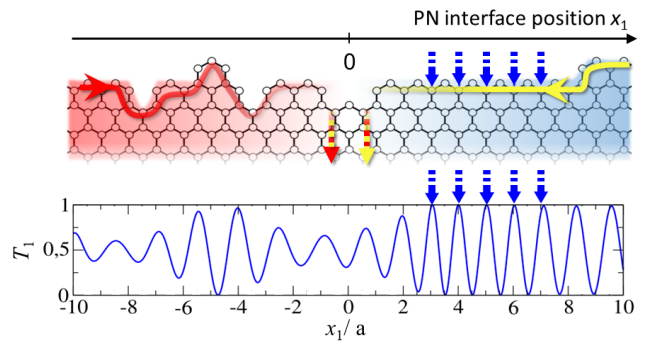


Figure 3: **Numerical simulations of the quantum Hall valley splitter.** Transmission T_1 calculated with KWANT as a function of the position x_1 of the intersection between the PN interface and the top sample edge. Top panel: edge configuration used in the calculations. Only the edge channels participating in valley splitter are shown (red and yellow arrows). Bottom panel: resulting calculated transmission. For a clean zigzag edge (positive x_1), T_1 shows regular oscillations with the interface position, having the same period as the zigzag edge structure (blue dashed arrows). For a rough edge (negative x_1), the oscillations are irregular, both in period and in amplitude.

average. Combining this and the Aharonov-Bohm oscillation in Fig. 4b, we discuss later that ΔV_1 makes the PN-interface shift by ~ 1 nm below the top side gate. The period of the B dependence is $\Delta B_1 \sim 300$ mT, which corresponds to ~ 0.2 nm change of the magnetic length around $B = 9.2$ T. These lengths are comparable with the interatomic distance 0.142 nm of the pristine graphene and the period of atomic edge structures (e.g., 0.246 nm of the zigzag edge), and much shorter than the scale of spatial variation of gate-voltage induced electrostatic potential. This strongly suggests that the transmission T_1 is controlled by the atomic structure at the top intersection. The PN-interface shift is estimated from the experimental data, without the help of dedicated numerical simulations. This direct estimation is possible with independent control of the top and bottom side gates and could not be done in previous works [16, 17]. We also measure the transmission probability $T_2 = I_T / (I_0/2)$ of the junction as a function of the voltage V_2 applied on the bottom side gate, when the filling factor below the top (bottom) side gate is $\nu_1 = 0$ ($\nu_2 \leq -1$). In this case, valley-channel splitting occurs not at the top intersection but at the bottom; the spin-down injected current flows along the N side of the PN interface after passing the top intersection, and then flows, after passing the bottom intersection, to the bottom left edge with probability T_2 or to the bottom right with probability $1 - T_2$. Reproducible irregular oscillations in T_2 are also observed, as shown in Fig. 2c.

The irregular but reproducible oscillations in the transmissions are attributed to the atomic structure of the

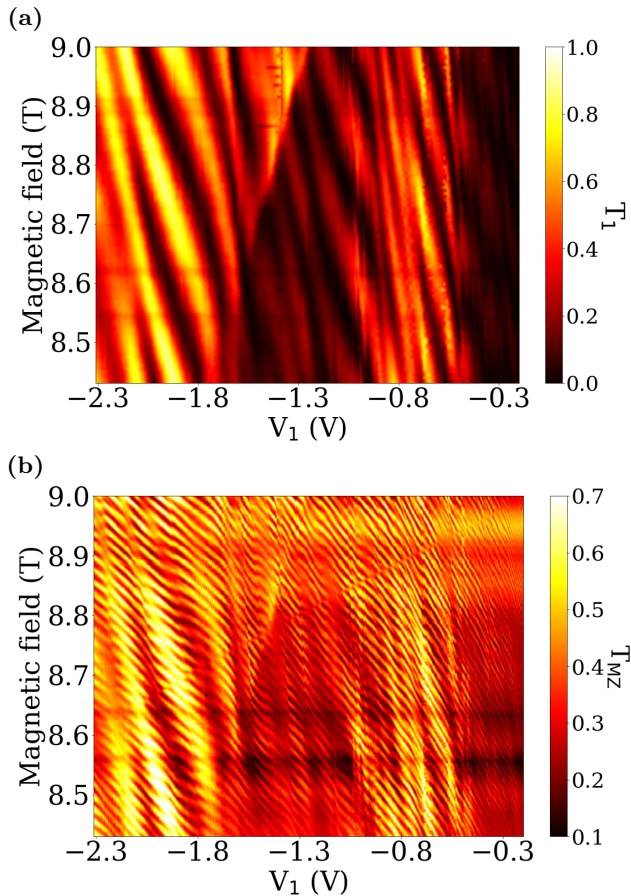


Figure 4: **Oscillations of the Mach-Zehnder interferometer.** (a) Measured T_1 as a function of V_1 and the magnetic field B , with the filling factor below the bottom side gate set to $\nu_2 = 0$ ($V_2 = 0.45$ V). We observe irregular oscillations of the transmission between 0 and near unity, with periods is $\Delta V_1 \sim 100$ meV and $\Delta B_1 \sim 300$ mT. (b) Measured device transmission T_{MZ} in the same range of V_1 and B , with $\nu_2 \leq -1$, forming a Mach-Zehnder interferometer.

intersection between the PN interface and the sample's edge. This is supported by our numerical calculations (see Fig.3, and Appendix E) using the KWANT quantum simulation software[21]. The transmission T_1 is computed in the vicinity of the top edge while varying the position x_1 of the top intersection. This corresponds to a change in the top side gate voltage V_1 . For a clean zigzag edge ($x_1 > 0$ in Fig.3), T_1 shows regular oscillations as a function of x_1 , with a period $a = 0.246$ nm matching the atomic-structure period of the zigzag edge. The oscillation is irregular when roughness is added along the top edge ($x_1 < 0$), but it has periods not much modified from the clean case. Disorder yields similar results, discussed in Appendix E. Our simulations are qualitatively compatible with the experimental data.

IV. TUNABLE MACH-ZEHNDER INTERFEROMETER

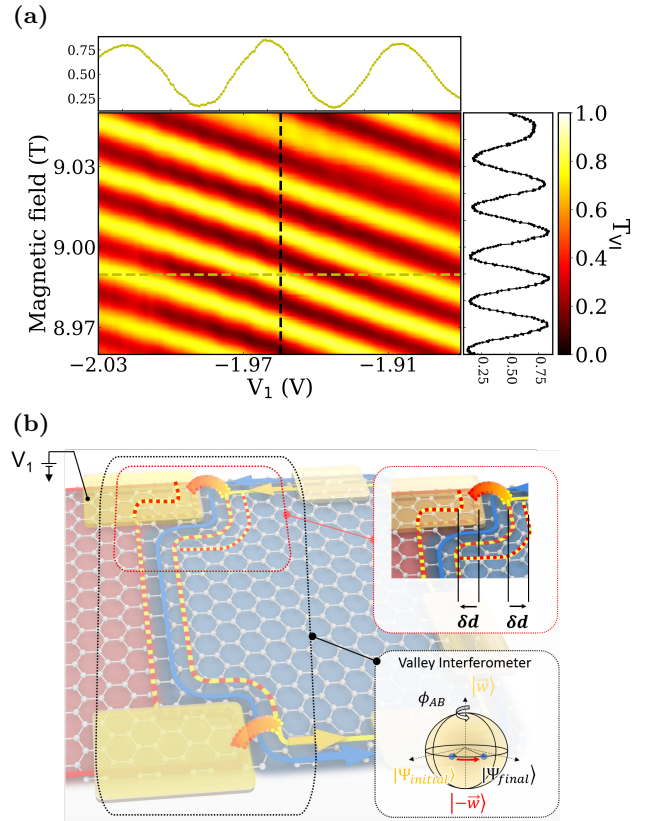


Figure 5: **Controlling the Mach-Zehnder interferences with the quantum Hall valley splitter** (a) T_{MZ} as a function of B and V_1 with $T_1 = T_2 \sim 1/2$. (b) Widening of the spatial separation $2\delta d$ between the interface channels in the region below the top side gate due to change ΔV_1^{MZ} of the gate voltage. (inset) Equivalence of the interference and the rotation of a flying valley-isospin state on the Bloch sphere. When the azimuthal angle is chosen to be $\pi/2$ (the top valley splitter is half-open as $T_1 = |t_1|^2 = 0.5$), the valley isospin of the initial state $|\Psi_{\text{initial}}\rangle = (|\downarrow, \vec{w}\rangle + e^{i\theta}|\downarrow, -\vec{w}\rangle)/\sqrt{2}$ rotates around the z-axis by the polar angle ϕ_{AB} .

By tuning the filling factor below both the top and bottom side gates to $\nu \leq -1$, we have two valley splitters in series. Combining them, we further characterize and control the valley splitting and valley isospin. This is illustrated in Fig. 4, where we compare the device transmission T_1 when the filling factor below the bottom side gate is set to $\nu_2 = 0$ (Fig. 4a) to the transmission $T_{MZ} = I_T/(I_0/2)$ when $\nu_2 \leq -1$ (Fig. 4b). Strikingly, we observe regular, smaller scale oscillations in T_{MZ} ($\Delta B^{MZ} \sim 25$ mT, and $\Delta V_1^{MZ} = 50$ meV) that are super-

imposed to the larger scale oscillations of T_1 shown in Fig. 4a.

These oscillations are naturally interpreted as interference fringes of a Mach-Zehnder interferometer where the interface channels $|\downarrow, \pm\tilde{w}\rangle$ constitute the two interferometer arms and the valley splitters behave as the beam splitters. From the Aharonov-Bohm phase $\phi_{AB} = 2\pi BA/\Phi_0$, $\Phi_0 = h/e$ being the flux quantum, we get the interferometer area $A = \Phi_0/\Delta B^{MZ} = 0.15 \mu\text{m}^2$ and the spatial separation of 110 nm between the two interface channels, given the length $1.5 \mu\text{m}$ of the PN interface. The separation results from electron-electron interactions [16].

The period $\Delta V_1^{MZ} = 50 \text{ meV}$ indicates that the interferometer area A is tuned by V_1 . The gate voltage V_1 generates potential to the P side and the N side asymmetrically, resulting in change δs of the spatial separation between the interface channels and shift $\delta d \sim \delta s/2$ of the PN interface below the top side gate (as depicted in Fig.5b). We estimate $\delta s \sim 1 \text{ nm}$, hence $\delta d \sim 0.5 \text{ nm}$, for $\Delta V_1^{MZ} = 50 \text{ meV}$ from the Aharonov-Bohm flux $\delta s L_s B = \Phi_0$ of the area $\delta s L_s$ at $B = 9.2 \text{ T}$ with the side-gate length $L_s = 450 \text{ nm}$. This implies that $\Delta V_1 = 100 \text{ meV}$ applied on the top side gate voltage V_1 enables to shift the PN interface by a distance of $\delta d \sim 1 \text{ nm}$, supporting that the dependence of T_1 on V_1 in Fig.2 is related with the valley isospin. The two measurements in Figs. 4a and b are perfectly consistent and confirm our interpretation. We remark that independent control of the two valley splitters is crucial for characterization of the valley splitters and the Mach-Zehnder interferometers, as there are multiple periodicities of different origin such as ΔB_1 , ΔB^{MZ} , ΔV_1 , and ΔV_1^{MZ} . This was not achieved previously [16, 17].

We provide a theoretical understanding for the transmission probability T_{MZ} . The valley superposition in Eq. (1) further evolves, gaining the Aharonov-Bohm phase, into a state $|\Psi_{\text{final}}\rangle = r_1|\downarrow, \tilde{w}\rangle + t_1 e^{i\phi_{AB}}|\downarrow, -\tilde{w}\rangle$ at the interface bottom. This happens when there is no atomic defect along the PN interface (as in our experiment, AB oscillations being extremely robust over a wide parameter range of the magnetic field and gate voltage) so that the valley isospin $\pm\tilde{w}$ does not change. Therefore, the valley superposition is further engineered by using the Aharonov-Bohm effect. On the other hand, the bottom valley splitter is characterized by a scattering eigenstate [12, 13] $|\tilde{\Psi}\rangle$ of the interface that perfectly goes to the left-moving bottom edge channel; the state orthogonal to $|\tilde{\Psi}\rangle$ moves to the right-moving channel. We write this state as $|\tilde{\Psi}\rangle = t_2|\downarrow, \tilde{w}\rangle + r_2|\downarrow, -\tilde{w}\rangle$ with amplitudes r_2 and t_2 satisfying $|r_2|^2 + |t_2|^2 = 1$, choosing the interface states $|\downarrow, \pm\tilde{w}\rangle$ as basis states. The transmission probability is obtained as $T_{MZ} = |\langle \tilde{\Psi} | \Psi_{\text{final}} \rangle|^2 = |r_1 t_2^* + t_1 r_2^* e^{i\phi_{AB}}|^2$,

$$T_{MZ} = |r_1 t_2|^2 + |r_2 t_1|^2 + 2|r_1 t_1 r_2 t_2| \cos(\phi_{AB} + \phi), \quad (2)$$

where $\phi = \arg(t_1 t_2 r_1^* r_2^*)$ can include the dynamical phase. This has the standard form of the Mach-Zehnder interference, but includes the effect of the valley isospin.

We study the interference visibility $(T_{MZ,\text{max}} - T_{MZ,\text{min}})/(T_{MZ,\text{max}} + T_{MZ,\text{min}})$, where $T_{MZ,\text{max}(\text{min})}$ is the

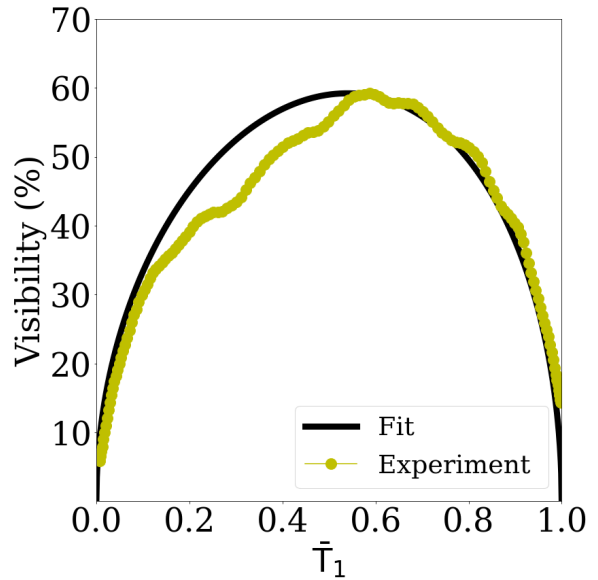


Figure 6: **Transmission dependence of the Mach-Zehnder visibility.** Interference visibility as a function of the normalized \bar{T}_1 (see Appendix D). The visibility (yellow dots) of the experimentally measured oscillation of T_{MZ} and the curve of $\alpha\sqrt{\bar{T}_1(1-\bar{T}_1)}$ where α is an adjustable parameter show good agreement.

maximum (minimum) value of the oscillation of T_{MZ} . To obtain the largest visibility, we first set the bottom side gate to $\nu_2 = 0$ and tune V_1 to get $T_1 \sim 1/2$. Next we set the bottom side gate to $\nu_2 \leq -1$ and finely tune V_2 to reach the maximum visibility. According to Eq. (2), we expect the visibility $\propto \sqrt{T_1(1-T_1)}$. This behavior is found in Fig.6. The excellent agreement between the experimental visibility and the $\sqrt{T_1(1-T_1)}$ law obtained with the independent measurement of T_1 supports the formation of the Mach-Zehnder valley interferometer and confirms the coherence of the valley superposition in Eq. (1). The analysis indicates that the valley isospin direction of the superposition $|\Psi_{\text{final}}\rangle$ is tuned over the range of $|t_1|^2 = 0.018 - 0.812$ and $\phi_{AB} = 0 - 2\pi$ with changing V_1 and B . Hence the valley splitters enable the basic operations of a valley-isospin state, its rotation over the almost whole parameter range (see in Fig.5b inset).

V. COHERENCE PROPERTIES OF THE VALLEY-SPLIT STATE

In the last section, we address the coherence properties of the valley-split states propagating along the PN interface when electrons are injected at higher energy. In Fig.7a, T_{MZ} is represented as a function of the applied bias voltage and the magnetic field. We observe a lobe-type structure which is accompanied by a phase shift of π when then visibility is canceled. This behavior has already been observed in Mach-Zehnder interferometers realized in GaAs/AlGaAs heterostructures [22]. We as-

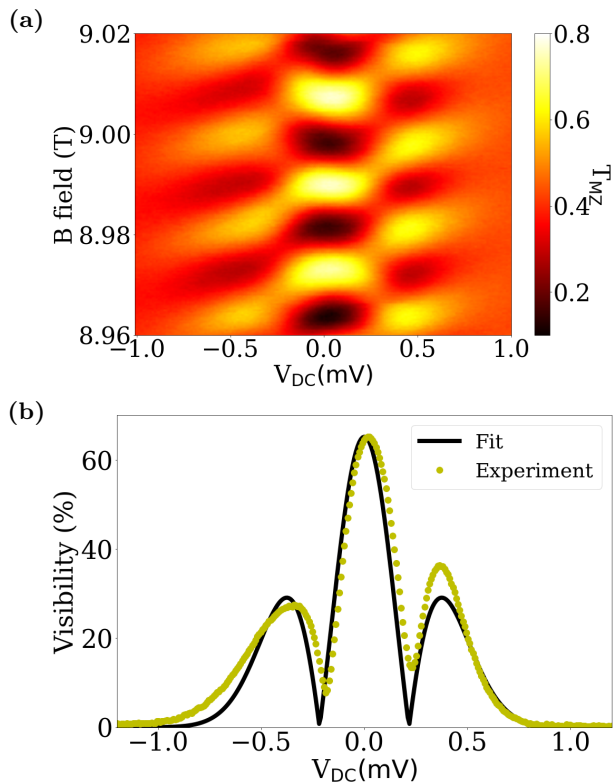


Figure 7: **Energy dependence of the Mach-Zehnder visibility.** (a) T_{MZ} as a function of the DC bias V_{DC} (applied to the upper right ohmic contact for the injection of I_0) and the magnetic field. (b) Measured visibility (yellow dots) as a function of V_{DC} . Computed visibility (black solid line) based on gaussian phase fluctuations is in agreement with the experimental data.

sume a Gaussian distribution of the phase $\varphi = \phi_{AB} + \phi$ (see Eq.2) with a variance $\langle \delta\varphi^2 \rangle = V_{DC}^2/V_{lob}^2$ where $\langle \rangle$ denotes the average over the phase distribution and V_{lob} is an adjustable parameter. This approach leads to a visibility $\propto e^{-V_{DC}^2/V_{lob}^2} |1 - V_{DC}^2/V_{lob}^2|$ (black solid line in Fig.7b) [23]. Most of the models developed to account for side lobe patterns in GaAs/AlGaAs heterostructures rely on the partitioning induced by the first beam splitter [24, 25]. Experimentally a clear dependence of the lobe structure has been observed as a function of the transmission of the first beam splitter [26]. Unexpectedly, we do not observe such a dependence in graphene (see *e.g.* Appendix Fig. 16). Further systematic studies on this issue are currently ongoing. Still, it is remarkable to note that in graphene $V_{lob} = 217 \mu\text{eV}$, which is 20 times larger than usual values reported in GaAs/AlGaAs heterostructures.

VI. CONCLUSION

To conclude, we have demonstrated that monolayer graphene in the quantum Hall regime is a promising platform to perform electron quantum optics experiments. We have first characterized a quantum Hall valley splitter showing that the valley mixing between two opposite valley isospin edge states can be finely tuned. Coherence of this valley beam splitter is discussed by implementing it in a PN-junction to define a fully tunable electronic Mach-Zehnder interferometer. This new type of quantum-coherent valleytronics devices should allow to envision two-valley-state operations and entanglement schemes[27]. Moreover, the valley splitters play the role of a gate-tunable quantum point contact, an elementary device whose realization in monolayer graphene is missing due to Klein tunneling [28], between quantum Hall edge channels. The demonstration of quantum coherent valleytronics opens another large field of quantum transport devices in graphene including quantum dots, Kondo impurities, and various interferometers such as Fabry-Perot resonators.

ACKNOWLEDGMENTS

We warmly thank Thierry Jolicoeur and Mark Goerbig for enlightening discussions, as well as P. Jacques for technical support. This work was funded by the ERC starting grant COHEGRAPH, the CEA, the French Renatech program, “Investissements d’Avenir” LabEx PALM (ANR-10-LABX-0039-PALM) (Project ZerHall), and by the EMPIR project SEQUOIA 17FUN04 cofinanced by the participating states and the EU’s Horizon 2020 program. It is also supported by Korea NRF via the SRC Center for Quantum Coherence in Condensed Matter (GrantNo.2016R1A5A1008184).

[†] main corresponding author ^{††}co-corresponding author * equal contribution

VII. SUPPLEMENTARY MATERIAL

Appendix A: Sample fabrication

Graphene, hBN, and graphite flakes were mechanically exfoliated onto the surface of SiO₂/Si using the conventional scotch tape method. Graphene and graphite flakes were prepared by exfoliating bulk graphite from NGS Naturgraphit GmbH and hBN flakes were obtained by exfoliating bulk crystals from NIMS. By optical microscope, single-layer graphene was chosen. And this has been further confirmed with Raman spectroscopy after successful encapsulation with hBNs. By doing this we can avoid any spurious signature in the Raman spectrum of graphene [29]. All the crystals were carefully checked with optical microscopy and noncontact mode

AFM for any defect, contamination and inhomogeneity in thickness before stacking. Using the van der Waals (vdW) dry transfer method, graphene was encapsulated in hBNs [30]. Then this BN/graphene/BN stack was transferred on a flake of graphite (9nm), which is used as a back gate. Top BN=27nm, bottom BN = 33nm. The finished stack was annealed in vacuum at $\sim 350^\circ\text{C}$ to enhance the quality of the sample and then it was checked with noncontact mode AFM to locate bubbles and defects.

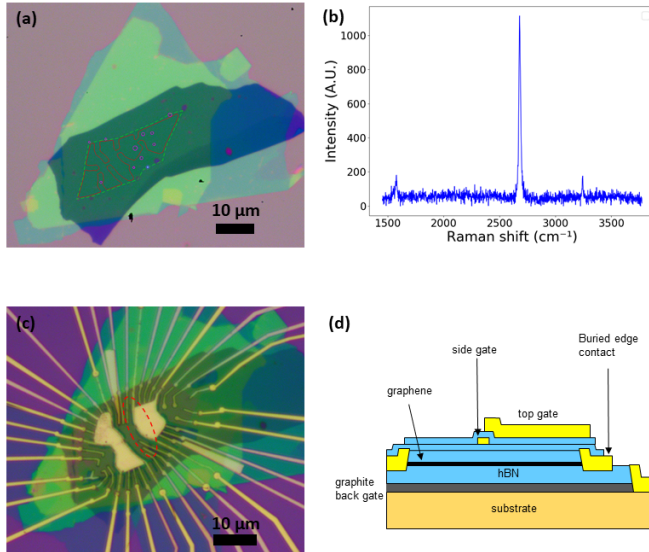


Figure 8: Sample description. (a) Optical image of BN/graphene/BN/graphite stack. The green dashed line indicates the edge of graphene. Red line indicates graphene mesa which would be defined by subsequent RIE etch. Purple circles indicate bubbles in the stack which later would be eliminated by ohmic contacts fabrication or mesa etching. (b) Raman spectroscopy of encapsulated single-layer graphene. This data was taken after successful encapsulation of graphene with top and bottom hBN but before adding additional graphite. We could minimize the spurious substrate effect and also avoid overlapping with the spectrum of graphite underneath. (c) Optical image of a finalized device. The dashed red line indicates one PN-junction, which defined by applying gate voltage from the graphite back gate and metallic top gate. (d) Cut plane view of the sample, equivalent of dashed red line section in (c)

Poly(methyl methacrylate) (PMMA) pattern defined by e-beam lithography was used as a mask for O₂/CHF₃ reactive ion etch (RIE) to expose the 1D edge of graphene. And using the same PMMA layer as a liftoff mask, edge contacts were defined by e-beam evaporating Cr/Au=10/30nm while rotating the sample using a tilted rotation stage. We etched the graphene channel into desired mesa geometry by using the same RIE procedure with PMMA resist mask. PMMA resist was cleanly removed in hot Acetone later. To prevent any

possible leakage between the exposed graphene edge and additional gates, 10nm hBN was picked up and dry transferred on top of the sample. When removing PPC, annealing was not used this time to avoid any possible degradation of ohmic contacts. Melted PPC was cleaned with hot Acetone. Side gates were defined by evaporating Cr/Au=10/30nm. An additional 15nm BN was picked up and dry transferred on top of the sample like described before. Then finally top gates were defined by evaporating Cr/Au=10/40nm (in Fig.8).

Appendix B: Sample geometry

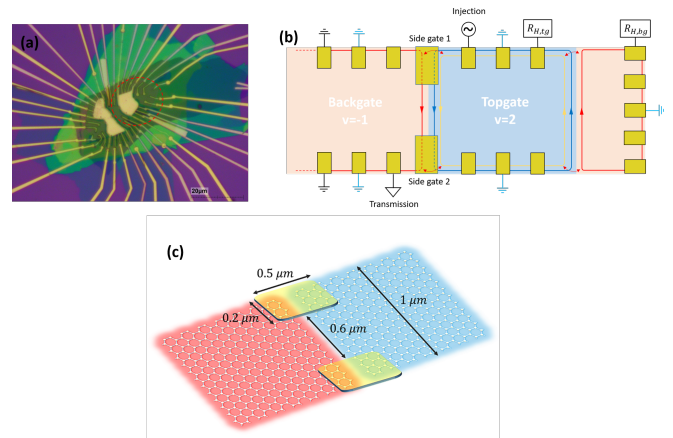


Figure 9: Sample geometry. (a) Optical micrograph of the finalized sample composed of two top gates (corresponding to the two golden plates in the center). The top gate used in this study is circled by a red dashed line. Two PN junctions are generated by the top gate : one on the right without side gates plays the role of a test sample, and another one on the left with side gates corresponds to the valley splitter sample. (b) Schematic of the used part of the sample (circled by the red dashed line in (a)). The n-doped region (blue) is set at filling factor $\nu = 2$. The p-doped region under the top gate (red) is at $\nu = -1$. On the left junction, current was injected from the top right contact, and the transmitted current was measured through the bottom left contact. Note that we could not measure the reflection as the bottom right contact is not working. Light blue grounds correspond to cold grounds. The two-point Hall resistance was measured under the top gate (denoted $R_{H,tg}$) and outside (denoted $R_{H,bg}$). (c) Characteristic dimensions of the valley splitter sample : the sample width $1.0\mu\text{m}$, the distance between the side gates $0.6\mu\text{m}$, and a total side gate length $L_s=450\text{nm}$.

The sample fabricated is composed of two top gates (in Fig.9(a)). Only the right top gate circled by a red dashed line has been used in this study. As shown in the schematic of the used part of the sample (in Fig.9(b)),

two PN junctions are generated by the top gate : one on the right without side gates plays the role of a test sample, and the other one on the left with side gates correspond to the valley splitter sample. Precise dimensions of the valley splitter sample are presented in Fig.9(c). The width of the graphene ribbon is $1.0\mu\text{m}$. The side gates are rectangles of length $0.20\mu\text{m}$ and width $0.5\mu\text{m}$ separated by distance $0.6\mu\text{m}$. Half of the side gates is below the top gate, this implies that the PN junction meets the side gates borders in their middle at a distance $0.25\mu\text{m}$ of the two other borders of each side gate. Electrons propagate along the edge of the side gate over a length $L_s=450\text{ nm}$. The total PN interface length is $2L_s+0.6=1.5\mu\text{m}$ as mentioned in the main text.

Appendix C: Current conservation

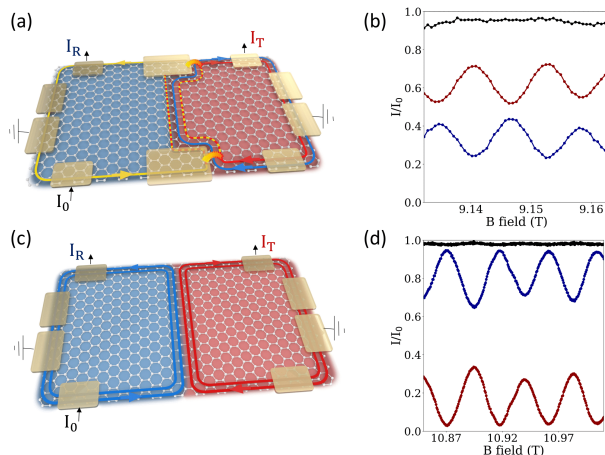


Figure 10: **Current conservation in two interferometers.** (a) Schematics representation of an interferometer with side gates (yellow). A current I_0 is injected on the n side (blue) at filling factor $\nu_N = 1$. After its transfer through the pn junction, we measure the reflected, I_R , and transmitted, I_T , current with two ohmic contacts (grey). Additional ohmic contacts are used as ground sinks. (b) Transmitted (red) and reflected (blue) current normalized by the injected current I_0 , as a function of magnetic field B . These current oscillate with opposite phase and their sum (black) is conserved. (c) Schematics representation of an interferometer without side gate. A current I_0 is injected on the n side (blue) at filling factor $\nu_N = 2$. (d) Transmitted (red) and reflected (blue) current normalized by the injected current I_0 , as a function of magnetic field B . These currents oscillate with opposite phase and their sum (black) is conserved.

We check experimentally that the injected current is equal to the sum of the reflected and transmitted current through the PN junction with the side gates (device described in the main text, see in Fig.10A). In the N region

the Landau-level filling factor is $\nu_N = 1$ and one spin-down channel circulates counterclockwise, while in the P region $\nu_P = -2$ and two channels of the opposite spin (\uparrow, \downarrow) circulates clockwise. As shown in Fig.10B, transmitted current in red is in phase opposition with the reflected current (in blue). Total current (in black) is conserved. Note that the AB periodicity of $B=12\text{mT}$ (Fig.10B) is two times smaller than described in the main text. In the main text, $(\nu_N, \nu_P)=(-1, +2)$ while here $(\nu_N, \nu_P)=(+1, -2)$. $(\nu_N, \nu_P)=(-1, +2)$ is reached with top gate voltage $V_{TG}=2.54\text{V}$ and back gate voltage $V_{BG}=-0.59\text{V}$ leading to a voltage difference $\Delta V_{G,1}=3.13\text{V}$. $(\nu_N, \nu_P)=(+1, -2)$ is reached with top gate voltage $V_{TG}=-2.16\text{V}$ and back gate voltage $V_{BG}=0.13\text{V}$ leading to a voltage difference $\Delta V_{G,2}=2.29\text{V}$. Ratio of these potential differences for the two opposite chirality is $\frac{\Delta V_{G,1}}{\Delta V_{G,2}}=1.37$, which leads to a sharper potential profile for $(\nu_N, \nu_P)=(-1, +2)$ than $(\nu_N, \nu_P)=(+1, -2)$ and a reduced distance between edge states. Fig.10C shows transmitted and reflected current for the test sample without side gates at $(\nu_N, \nu_P)=(+2, -2)$ (test sample). Total current (in black) is conserved. The AB periodicity is larger, in Fig.10D, mostly because the total length of the interferometer, $L=1\mu\text{m}$, is smaller, due to the absence of side gates.

Appendix D: Quantitative study of the visibility dependence on the transmission

In this part, we detail the experimental procedure to extract the interference visibility as a function of the normalized \bar{T}_1 as depicted in Fig.6 of the main text. As shown in Fig.4a of the main text, T_1 effectively oscillates with V_1 from 0 to near unity. However, T_1 also depends on the magnetic field B . Since the visibility is computed for a fixed T_1 , this latter needs to be constant with the magnetic field. A constant transmission while sweeping the magnetic field can be obtained by adding, for each magnetic field value B , a linear correction to the gate voltage $V_1(B) = aB + b$ (with a and b the computed coefficients). In Fig.11(a), the gate voltage $V_1(B)$ was swept around the corrected value $V_{1,\text{corr}}(B)$ following formula : $V_1(B) = V_{1,\text{corr}}(B) + \delta V_1$ with δV_1 going from -110 to 80mV . Thanks to this, an almost B-independent T_1 , going from 0.018 to 0.812 , is achieved as a function of the relative bias δV_1 . Since T_1 does not reach neither 1 nor 0, we introduce $\bar{T}_1 = (T_1 - T_{1,\text{min}})/(T_{1,\text{max}} - T_{1,\text{min}})$ (Fig.11(b)). This normalization procedure is based on the assumption that a part of the current is reflected at another point, and does not flow through the interferometer, explaining the lower value of the maximum transmission. An analogue assumption can be made to explain the slightly above zero minimum of the T_1 . Tuning $\nu_1 = 0$ below the top side gate and $\nu_2 \leq -1$ below the bottom side gate, we measure T_2 in the same B-range (see in Fig.11(c)). As shown in Fig.11(d), an almost constant value of $T_2 \sim 1/2$ with the magnetic field is observed by following the brown line in the B- V_2 space. Finally,

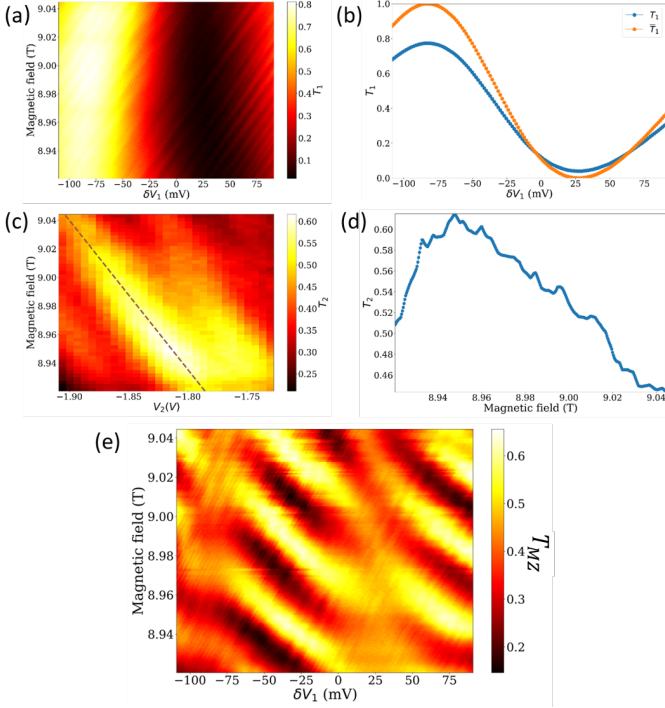


Figure 11: **Experimental settings for the measurement of the visibility dependence on T_1 .**

(a) Transmission T_1 of the top valley splitter as a function of the magnetic field and the bias δV_1 applied on it (while $\nu_2 = 0$). (b) Transmission T_1 averaged on the B-range as a function of δV_1 . \bar{T}_1 is the normalized value of T_1 defined by

$$\bar{T}_1 = (T_1 - T_{1,min}) / (T_{1,max} - T_{1,min})$$

with $T_{1,max}$ the maximum value of T_1 and $T_{1,min}$ its minimum. (c)

Transmission T_2 of the bottom valley splitter as a function of the magnetic field and the gate voltage V_2 (while $\nu_1 = 0$). (d) Transmission T_2 as a function of V_2 following the brown line in (c). (e) Transmission T_{MZ} of the valley interferometer as a function of the magnetic field B and the bias δV_1 on the top valley splitter, same B- δV_1 window as in T_1 measurement (figure (a)) with $T_2 \sim 1/2$ (figure (d)).

using these linear corrections, we measured, as shown in Fig.11(e), Aharonov-Bohm oscillations for a constant transmission T_2 as function of the relative gate voltage δV_1 (corresponding to fixed values of \bar{T}_1). For each \bar{T}_1 value, we compute the experimental visibility thanks to sinusoidal fits of the Aharonov-Bohm oscillations.

Appendix E: Numerical simulations

Hereafter, we study numerically the 3-terminal np junction sketched in Figs.12(a), 13(a), and 14(a) modeling a valley splitter with disorder (Figs.12(a) and 14(a)) or roughness (Fig.13(a)) along the physical edge. A graphene rectangular sample of length L and width W

is connected to two left and right horizontal leads of width W_h and to one top vertical lead of width L . The Zeeman term that lifts spin degeneracy is not taken into account. We use the spinless scaled tight-binding model of graphene [31] with interatomic distance $\tilde{a} = s_f \tilde{a}_0$ and nearest-neighbor hopping term $t = t_0/s_f$, where $\tilde{a}_0 = 0.142$ nm and $t_0 = 2.8$ eV are respectively the interatomic distance and the hopping term for real graphene while s_f is a scaling parameter. The Hamiltonian of the total system (including the leads) reads

$$H = - \sum_{\langle i,j \rangle} t e^{i\Phi_{ij}} c_i^\dagger c_j + \sum_i (V_i - \mu) c_i^\dagger c_i + \sum_{i \in \mathcal{B}} V_i^{dis} c_i^\dagger c_i \quad (\text{E1})$$

where c_i^\dagger and c_i are respectively the creation and annihilation operators of an electron at site $\mathbf{r}_i = (x_i, y_i)$, the sum $\sum_{\langle i,j \rangle}$ is restricted to nearest neighbors, and $\Phi_{ij} = (e/\hbar) \int_{\mathbf{r}_j}^{\mathbf{r}_i} \mathbf{A} \cdot d\mathbf{r}$ is the Peierls phase accounting for the presence of the perpendicular magnetic field $\mathbf{B} = \nabla \times \mathbf{A}$ applied everywhere. Note that technically, the expression of Φ_{ij} as a function of the spatial coordinates x_i, x_j, y_i and y_j depends on the choice of the electromagnetic gauge. In practice, the Landau gauge $\mathbf{A}(x, y) = -By \hat{x}$ is chosen in the horizontal leads while a rotated gauge $\mathbf{A}(x, y) = Bx \hat{y}$ is chosen in the vertical lead so as to guarantee that the expression of the Peierls phase is invariant by translation along the lead axis in all leads [32]. Inside the sample, we choose a gauge which interpolates smoothly between the two aforementioned gauges in order to avoid spurious reflections at the interface between the leads and the scattering region (this requires $W \gg W_h$). The second term on the right-hand side of Eq.(E1) mimics a np junction induced experimentally by the top/bottom gates and the side gate. μ is a constant potential applied everywhere and $V_i = V(\mathbf{r}_i)$ defined by

$$V(\mathbf{r}_i) = \frac{V_g}{2} \left[1 + \tanh \left(\frac{2(x_i - c(y_i))}{l} \right) \right], \quad (\text{E2})$$

interpolates from 0 in the left part ($x \ll 0$) to V_g in the right part ($x \gg 0$), over a characteristic length l . The position $c(y_i) = x_1 + \frac{x_0 - x_1}{2} [1 + \tanh[(2(y_i - L_{sg} + W/2)/l)]]$ of the np interface varies from x_1 (when it intercepts the sample boundary) to x_0 (deep inside the sample). Here L_{sg} is a parameter corresponding to the length of the side gate and the site of coordinates (0,0) is taken at the center of the sample. When $x_0 = x_1$, the np junction is translationally invariant (see Figs.12(a) and 13(a)) and the system models the valley splitter in the vicinity of the graphene physical edge. If $x_0 \neq x_1$, the np junction is twisted (see Fig.14(a)) and the modeled valley splitter includes the whole region from the physical edge to the end of the side gate. Finally, the last term in Eq.(E1) is a disordered potential applied only on the outermost sites at the bottom boundary edge \mathcal{B} inside the sample (and not in the leads). V_i^{dis} are random numbers uniformly distributed in $[-V_{dis}/2, V_{dis}/2]$.

In the following, we consider samples with zigzag edges along the x (horizontal) axis. Perfect edges are considered in Figs.12 and 14 while in Fig.13, roughness is added

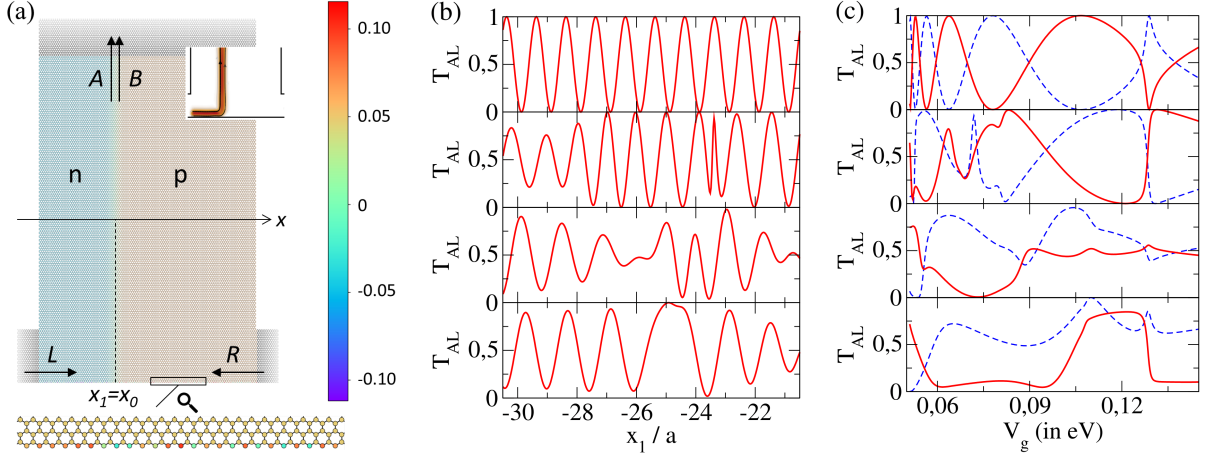


Figure 12: (a) Sketch of the translationally invariant np junction connected to 3 terminals. Two (spin-degenerate and) valley polarized edge states L and R coming from the left and the right lead respectively are scattered into two (spin-degenerate and) valley-degenerate states A and B at the np interface. The color scale shows the value of the potential on each site (in eV). The zoom-in to the boxed region at the bottom boundary highlights the disordered zigzag edge. The top right inset shows a 2D plot of the local current in the system, coming from the left lead. (b) Transmission T_{AL} as a function of the position $x_1 = x_0$ of the np interface. Data are shown for one given disorder configuration but different disorder amplitudes ($V_{dis} = 0, 0.25, 0.5,$ and 1 eV from top to bottom). The top and bottom panels correspond respectively to Fig.3a and b, within a narrower range of values of x_1 . (c) Same as (b) but T_{AL} is plotted as a function of the amplitude V_g of the np step at fixed $x_1 = x_0 = -50$ nm (red lines) and fixed $x_1 = x_0 = -50$ nm $+ a/2 \approx -49$ nm (blue dashed lines) (upon remaining in the regime $(\nu_N, \nu_P) = (2, -2)$). In all panels, $B = 10$ T, $\mu = 0.05$ eV, $s_f = 8$, $l = 10$ nm $\approx 5a$, $W = 300$ nm. In (a), $L = 200$ nm and $W_h = 50$ nm while in (b) and (c), $L = 280$ nm and $W_h = 70$ nm. In (b), $V_g = 0.11$ eV.

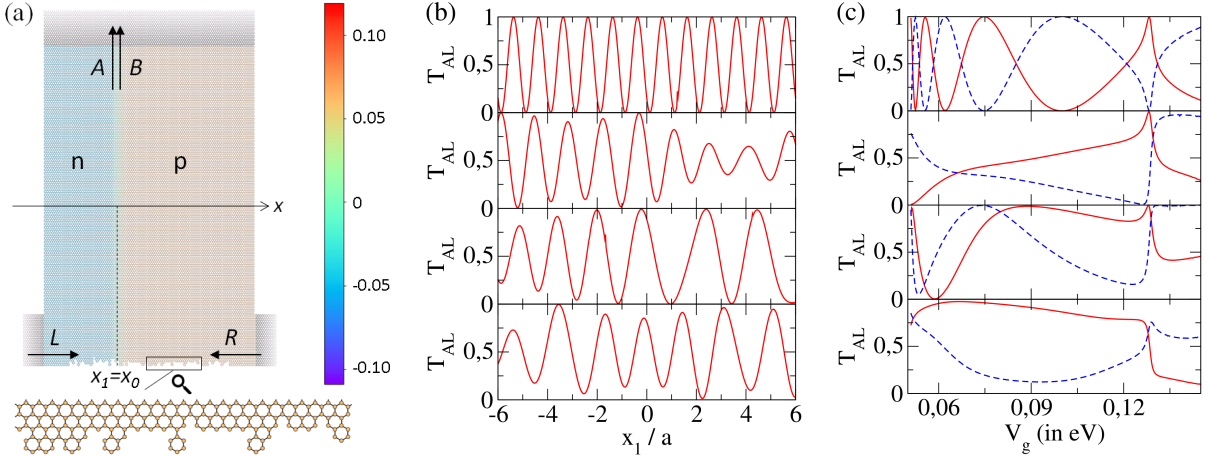


Figure 13: Same as Fig.12 by adding roughness at the zigzag bottom boundary (but no on-site disordered potential *i.e.* $V_{dis} = 0$). Near the np interface (and not in the leads), the y -position of the bottom boundary at x is taken as the maximum value between y_{min} (*i.e.* the y -position of the bottom boundary in the leads) and a random number drawn from a gaussian probability with standard deviation σ_r and center y_{min} . (a) Sketch of a sample with edge roughness ($\sigma_r = 2a$). (b) Transmission T_{AL} as a function of the position $x_1 = x_0$ of the np interface, for various roughness depths ($\sigma_r = 0, a, 2a,$ and $3a$ from top to bottom). (c) Same as (b) but T_{AL} is plotted as a function of the amplitude V_g of the np step at fixed $x_1 = x_0 = 0$ nm (red lines) and $x_1 = x_0 = a/2 \approx 1$ nm (blue dashed lines). All other parameters are the same as in Fig.12.

along the bottom physical edge. We fix the scaling factor to $s_f = 8$ and take $B = 10$ T, $\mu = 0.05$ eV and V_g between roughly 0.05 eV and 0.15 eV (the zero of energy being taken at the Dirac point at zero field). With this choice of parameters, the filling factors are respectively $\nu_N = 2$ and $\nu_P = -2$ in the left (N) and in the right (P) parts, upon restoring the twofold spin degeneracy. We note L the (spin-degenerate) edge state coming from the left lead, and R the one coming from the right lead. Along the np interface, a pair of valley-degenerate (and spin-degenerate) channels, denoted by A and B , co-propagate. Note that within our non-interacting model, A and B are superimposed on each other. Using the KWANT software [21], we compute the transmission probabilities T_{AL} and T_{BL} for a (spinless) electron at zero energy to be scattered from the state L to the state A or B . Obviously, $T_{AL} + T_{BL} = 1$. In the main paper, T_{AL} and T_{BL} are called reflection and transmission probabilities of the beam splitter.

In panels (b) of Figs.12, 13 and 14, the transmission T_{AL} is plotted as function of the position x_1 of the np interface for a translationally invariant np junction with disorder (Fig.12(b)) or roughness (Fig.13(b)) along the bottom edge, and for a twisted np junction with a disordered bottom edge (Fig.14(b)). When the bottom zigzag edge is clean ($V_{dis} = 0$) and perfect (no roughness), data are perfectly fitted by

$$T_{AL}(x_1) = \frac{1}{2} \left[1 + \cos \left(\frac{2\pi x_1}{\lambda_1} + \varphi_1 \right) \right] \quad (\text{E3})$$

where φ_1 is an adjustable phase and the period λ_1 equals $\lambda_1 = 3a$ for the twisted junction (top panels of Fig.14(b)) and $\lambda_1 = a$ for the translationally invariant one (top panel of Fig.12(b) and of Fig.13(b)), $a = s_f \sqrt{3} \times 0.142$ nm being the lattice spacing of the scaled model (fits are not shown). This oscillating behavior of the beam splitter transmission is a signature of the rotation of the valley isospin of the interface states induced by a shift of the position x_1 of the np interface [13]. Note that when the clean translationally invariant np junction is tuned to the symmetric point (so that the states A and B are perfectly centered around the np interface), $T_{AL} = 0$ [resp. 1] when the np interface position $x_1 = x_0$ intercepts an inner [resp. outer] carbon atom of the zigzag boundary (*i.e.* $x_0 = x_1 \equiv 0_{[a]}$ [resp. $a/2_{[a]}$] in our geometry). This is not perfectly the case in the top panels of Figs.12(b) and 13(b) because the chosen parameters $\mu = 0.05$ eV and $V_g = 0.11$ eV correspond to a np junction which is slightly asymmetric (and the above phase φ_1 depend on those parameters). The phase shift in the curves $T_{AL}(x_1)$ induced by a spatial shift of the center of mass of the interface states is clearly visible in the top left panel of Fig.15, where two symmetric and asymmetric configurations of the np junction are compared. Moreover, when disorder or roughness is added along the bottom zigzag edge (bottom panels of Figs.12(b), 13(b) and 14(b)), the periodic pattern of $T_{AL}(x_1)$ is lost but the transmission keeps oscillating between minimal and maximal values close to 0

and 1. Changing the disorder or edge configuration leads to plots of T_{AL} which are quantitatively different but qualitatively similar. This illustrates the fact that the transmission pattern $T_{AL}(x_1)$ is a fingerprint of the local edge configuration in the vicinity of the region where the np interface and the physical bottom edge intersect. This point is further highlighted in Fig.15.

Besides, when the positions x_0 and x_1 of the np interface are fixed, we find that the transmission T_{AL} plotted as a function of the height V_g of the np potential step also oscillates between 0 and 1 in an apparent erratic way (Figs.12(c), 13(c) and 14(c)). We interpret these oscillations as follows. When V_g is varied (so as to remain in the regime $(\nu_N, \nu_P) = (2, -2)$), the position of the (superimposed) interface states A and B is shifted along x and their valley isospin rotate, which results in a variation of T_{AL} . Experimentally, x_0 , x_1 , and V_g are varied simultaneously by tuning the gate voltages. A more advanced theoretical description should account for the mixed quantum-electrostatic problem [33] to extract the model parameters from the experimental configurations. This is left for future works.

As a side comment, let us add that all data shown in Figs.12, 13, 14, and 15 have been obtained with a characteristic length $l = 10$ nm $\approx 5a$ for the np step (a being defined here for the scaled model, see above). We have reproduced (up to a shift along the x -axis) the oscillations of period a and $3a$ shown in the top panels of Figs.12(b), 13(b), and 14(b) for different values of l ranging from $l = 2$ nm $\approx a$ to $l = 25$ nm $\approx 12.7a$ (data not shown). The latter value is still much smaller than in experiments, yet numerical instabilities occurring for large l as well as finite-size effects hinder further numerical investigations. We expect the oscillations of period a of $T_{AL}(x_1)$ (corresponding to the translationally invariant junction) to be robust for large l since even a smooth np interface is predicted to induce intervalley scattering near a physical zigzag edge [34]. On the contrary, we expect the oscillations of period $3a$ of $T_{AL}(x_1)$ (corresponding to the twisted junction) to be modified as l becomes large enough not to induce intervalley scattering in the (bulk) region where the np interface changes direction.

Appendix F: Transmission dependence of the Visibility

Most of the models developed to account for side lobe pattern in GaAs/AlGaAs heterostructures rely on the partitioning induced by the first beam splitter [24, 25]. In Ref. [24], dephasing in electronic Mach-Zehnder interferometer is described taking into account Coulomb interactions between co-propagating edge states leading to a separation of the spectrum of edge excitations on slow and fast mode. This coupling strongly depends on the first beam splitter transmission. In the weak tunneling regime ($T_1 \ll 1$), a lobe structure of the visibility as a function of the bias is predicted but not in the weak

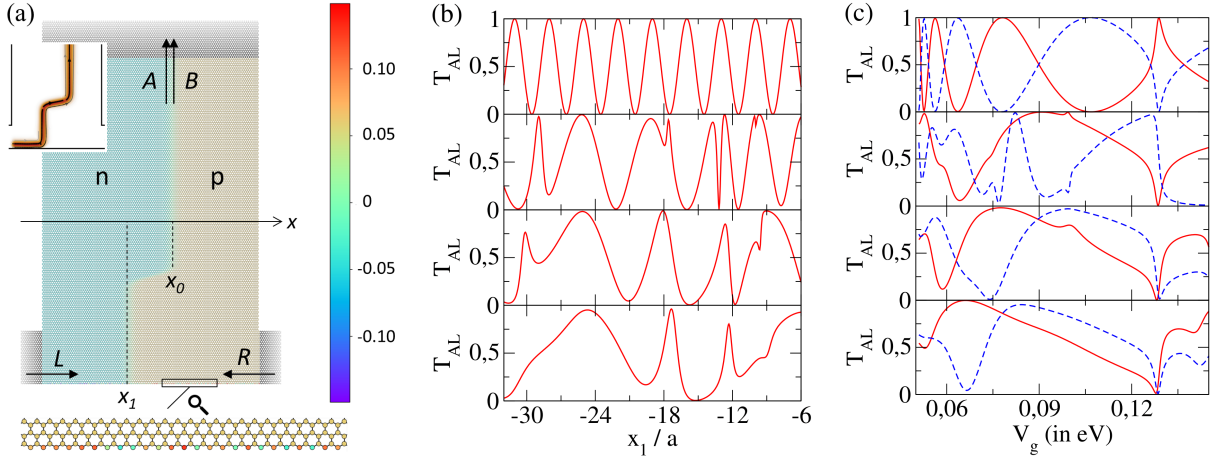


Figure 14: Same as Fig.12 for a twisted np junction (a). The transmission T_{AL} is plotted as a function of the position x_1 of the bottom np interface at fixed $x_0 = 50$ nm (b) and as a function of V_g (c) at fixed $x_0 = 30$ nm, $x_1 = -30$ nm (red lines) and at fixed $x_0 = 30$ nm, $x_1 = -30$ nm + $3a/2 \approx -27$ nm (blue dashed lines), for different disorder amplitudes ($V_{dis} = 0, 0.25, 0.5,$ and 1 eV from top to bottom). All other parameters are the same as in Fig.12 with additionally $L_{sg} = 100$ nm. Note that T_{AL} is independent of (finite) L_{sg} as long as $L_{sg} \gg 2l_B$ (l_B being the magnetic length).

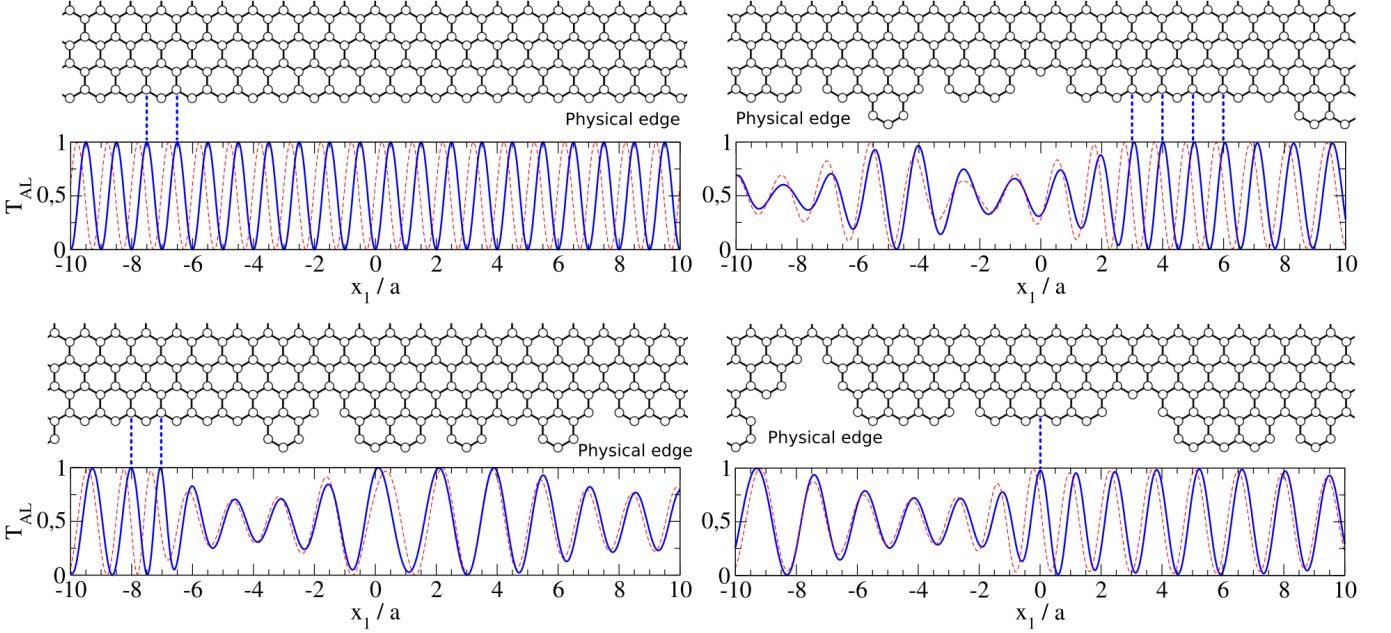


Figure 15: Transmission T_{AL} as a function of the position $x_1 (= x_0)$ of the np interface, for four edge configurations (shown on top of each panel). Data are shown for a symmetric np junction (blues lines, $\mu = 0.05$ eV and $V_g = 0.1$ eV) and for an asymmetric one (red dashed lines, $\mu = 0.06$ eV and $V_g = 0.1$ eV). The blue vertical dashed lines highlight the regions where the edges are locally of zigzag-type and T_{AL} is given (or well approximated) by Eq.(E3) (with $\lambda_1 = a$). In all panels, $B = 10$ T, $V_{dis} = 0$, $s_f = 8$, $l = 10$ nm $\approx 5a$, $W = 300$ nm, $L = 200$ nm, and $W_h = 70$ nm.

backscattering regime ($T_1 \gg 1$). In Ref.[25], the shot noise at the first beam splitter of the interferometer is considered. It is shown that shot noise generates an ensemble of nonequilibrium electron density configuration resulting in a lobe pattern in the visibility where minima of the lobe pattern strongly depends on T_1 . Experimentally, Ref. [26] reports clear dependence of the lobe structure of the visibility as a function of T_1 . Here we

do not observe such a dependence (in Fig.16) suggesting that decoherence mechanisms are different in graphene and GaAs/AlGaAs heterostructures.

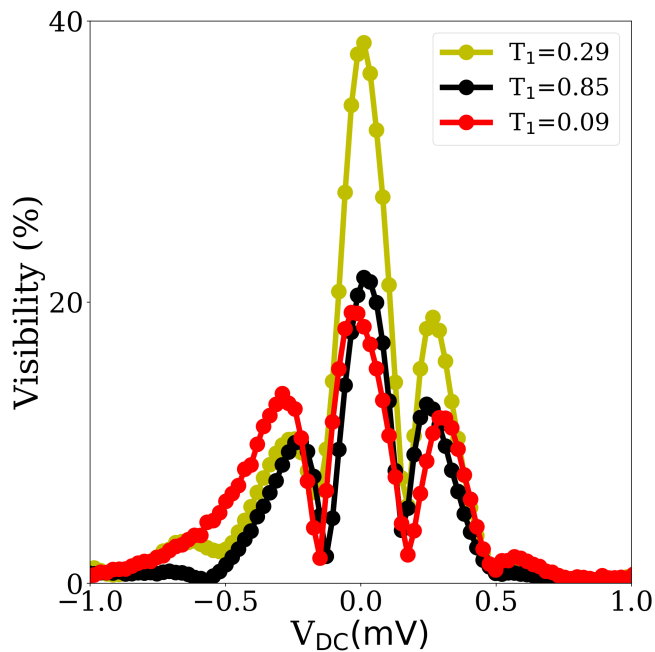


Figure 16: **Transmission dependence of the visibility.** Measured visibility as a function of V_{DC} for three different transmissions of the first valley splitter.

Appendix G: Temperature dependence of the interference oscillations

Temperature dependence of the interference oscillations is shown in Fig. 17. Interference oscillations are still visible at 1.5K which is very high compared to conventional GaAs/AlGaAs two-dimensional electron systems where interferences are typically washed out at 100mK [3].

Appendix H: Measurement

We used a Cryoconcept dry dilution refrigerator with a base temperature of 13mK. Measurements of transmitted currents and R_{Hall} values were performed using multiple Lock-in amplifiers with low noise preamplifiers. AC excitations 1nA-5nA with different frequencies (70Hz-300Hz) were used. Buried ohmic contacts underneath top gates enabled us the direct determination of filling factors from regions of interest.

-
- [1] C. Bäuerle, D. C. Glattli, T. Meunier, F. Portier, P. Roche, P. Roulleau, S. Takada, and X. Waintal, *Rep. Prog. Phys.* **81**, 056503 (2018).
- [2] Y. Ji, Y. Chung, D. Sprinzak, M. Heiblum, D. Mahalu, and H. Shtrikman, *Nature* **422**, 415 (2003).
- [3] P. Roulleau, F. Portier, P. Roche, A. Cavanna, G. Faini, U. Gennser, and D. Mailly, *Phys. Rev. Lett.* **100**, 126802 (2008).
- [4] C. Cabart, B. Roussel, G. Fève, and P. Degiovanni, *Phys. Rev. B* **98**, 155302 (2018).
- [5] C. W. J. Beenakker, *Rev. Mod. Phys.* **80**, 1337 (2008).
- [6] J. Schaibley, H. Yu, G. Clark, P. Rivera, J. S. Ross, K. L. Seyler, W. Yao, and X. Xu, *Nat. Rev. Mater.* **1**, 16055 (2016).
- [7] K. F. Mak, K. L. McGill, J. Park, and P. L. McEuen, *Science* **344**, 1489 (2014).
- [8] Y. Shimazaki, M. Yamamoto, I. Borzenets, K. Watanabe, T. Taniguchi, and S. Tarucha, *Nature Phys.* **11**, 1032 (2015).
- [9] L. Ju, Z. Shi, N. Nair, Y. Lv, C. Jin, J. Velasco Jr, C. Ojeda-Aristizabal, H. A. Bechtel, M. C. Martin, A. Zettl, J. Analytis, and F. Wang, *Nature* **520**, 650 (2015).
- [10] J. Li, R.-X. Zhang, Z. Yin, J. Zhang, K. Watanabe, T. Taniguchi, C. Liu, and J. Zhu, *Science* **362**, 1149 (2018).
- [11] R. V. Gorbachev, J. C. W. Song, G. L. Yu, A. V. Kretinin, F. Withers, Y. Cao, A. Mishchenko, I. V. Grigorieva, K. S. Novoselov, L. S. Levitov, and A. K. Geim, *Science* **346**, 448 (2014).
- [12] J. Tworzydło, I. Snyman, A. R. Akhmerov, and C. W. J. Beenakker, *Phys. Rev. B* **76**, 035411 (2007).
- [13] L. Trifunovic and P. W. Brouwer, *Phys. Rev. B* **99**, 205431 (2019).
- [14] Q. Ma, F. D. Parmentier, P. Roulleau, and G. Fleury, *Phys. Rev. B* **97**, 205445 (2018).
- [15] S. Morikawa, S. Masubuchi, R. Moriya, K. Watanabe, T. Taniguchi, and T. Machida, *Appl. Phys. Lett.* **106**, 183101 (2015).
- [16] D. S. Wei, T. van der Sar, J. D. Sanchez-Yamagishi, K. Watanabe, T. Taniguchi, P. Jarillo-Herrero, B. I. Halperin, and A. Yacoby, *Science Advances* **3** (2017), 10.1126/sciadv.1700600.
- [17] C. Handschin, P. Makk, P. Rickhaus, R. Maurand, K. Watanabe, T. Taniguchi, K. Richter, M.-H. Liu, and C. Schönenberger, *Nano Lett.* **17**, 5389 (2017).
- [18] P. Makk, C. Handschin, E. Tóvári, K. Watanabe, T. Taniguchi, K. Richter, M.-H. Liu, and C. Schönenberger, *Phys. Rev. B* **98**, 035413 (2018).
- [19] D. S. Wei, T. van der Sar, S. H. Lee, K. Watanabe, T. Taniguchi, and B. I. H. A. Yacoby, *Science* **362**, 229 (2018).
- [20] A. F. Young, C. R. Dean, L. Wang, H. Ren, P. Cadden-Zimansky, K. Watanabe, T. Taniguchi, J. Hone, K. L. Shepard, and P. Kim, *Nature Phys.* **8**, 550 (2012).
- [21] C. W. Groth, M. Wimmer, A. R. Akhmerov, and X. Waintal, *New J. Phys.* **16**, 063065 (2014).
- [22] I. Neder, M. Heiblum, Y. Levinson, D. Mahalu, and V. Umansky, *Phys. Rev. Lett.* **96**, 016804 (2006).
- [23] P. Roulleau, F. Portier, D. C. Glattli, P. Roche, A. Cavanna, G. Faini, U. Gennser, and D. Mailly, *Phys. Rev. B* **76**, 161309 (2007).
- [24] I. P. Levkivskiy and E. V. Sukhorukov, *Phys. Rev. B* **78**, 045322 (2008).

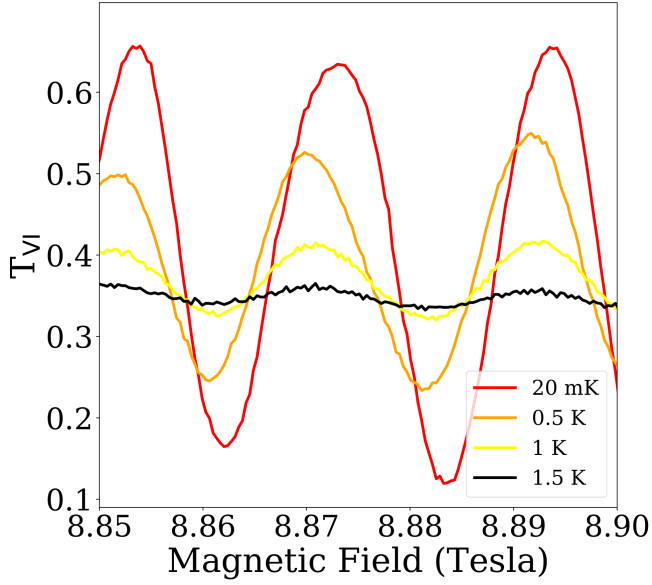


Figure 17: **Temperature dependence of the interference oscillations.** Measured T_{MZ} as a function of the magnetic field for different temperatures. At 1.5K, interference oscillations are still visible.

- [25] S.-C. Youn, H.-W. Lee, and H.-S. Sim, Phys. Rev. Lett. **100**, 196807 (2008).
- [26] E. Bieri, M. Weiss, O. Göktaş, M. Hauser, C. Schönenberger, and S. Oberholzer, Phys. Rev. B **79**, 245324 (2009).
- [27] P. Samuelsson, E. V. Sukhorukov, and M. Büttiker, Phys. Rev. Lett. **92**, 026805 (2004).
- [28] M. Katsnelson, K. Novoselov, and A. Geim, Nature Phys. **2**, 620 (2006).
- [29] F. Pizzocchero, L. Gammelgaard, B. Jessen, J. M. Caridad, L. Wang, J. Hone, P. Bøggild, and T. J. Booth, Nat. Commun. **7**, 11894 (2016).
- [30] L. Wang, I. Meric, P. Y. Huang, Q. Gao, Y. Gao, H. Tran, T. Taniguchi, K. Watanabe, L. M. Campos, D. A. Muller, J. Guo, P. Kim, J. Hone, K. L. Shepard, and C. R. Dean, Science **342**, 614 (2013).
- [31] M.-H. Liu, P. Rickhaus, P. Makk, E. Tóvári, R. Maurand, F. Tkatschenko, M. Weiss, C. Schönenberger, and K. Richter, Phys. Rev. Lett. **114**, 036601 (2015).
- [32] O. Shevtsov, P. Carmier, C. Petitjean, C. Groth, D. Carpentier, and X. Waintal, Phys. Rev. X **2**, 031004 (2012).
- [33] P. Armagnat, A. Lacerda-Santos, B. Rossignol, C. Groth, and X. Waintal, SciPost Phys. **7**, 31 (2019).
- [34] A. R. Akhmerov, J. H. Bardarson, A. Rycerz, and C. W. J. Beenakker, Phys. Rev. B **77**, 205416 (2008).